A prototype protein nanocage minimized from carboxysomes with gated oxygen permeability

Ruimin Gao[a,b,1], Huan Tan[b,c,1], Shanshan Li[d,e,1], Shaojie Ma[b,c], Yufu Tang[f], Kaiming Zhang[d,e], Zhiping Zhang[a], Quli Fan[f], Jun Yang[b,c,2], Xian-En Zhang[b,g,h,2], and Feng Li[a,b,2]

[a]State Key Laboratory of Virology, Wuhan Institute of Virology, Center for Biosafety Mega-Science, Chinese Academy of Sciences, Wuhan 430071, People's Republic of China; [b]University of Chinese Academy of Sciences, Beijing 100049, People's Republic of China; [c]National Center for Magnetic Resonance in Wuhan, Key Laboratory of Magnetic Resonance in Biological Systems, State Key Laboratory of Magnetic Resonance and Atomic and Molecular Physics, Wuhan Institute of Physics and Mathematics, Chinese Academy of Sciences, Wuhan 430071, People's Republic of China; [d]Key Laboratory for Cellular Dynamics, Ministry of Education, University of Science and Technology of China, Hefei 230027, People's Republic of China; [e]Department of Bioengineering, Stanford University, Stanford, CA 94305; [f]Key Laboratory for Organic Electronics and Information Displays, Jiangsu Key Laboratory for Biosensors, Institute of Advanced Materials, Jiangsu National Synergetic Innovation Center for Advanced Materials, Nanjing University of Posts and Telecommunications, Nanjing 210023, People's Republic of China; [g]Faculty of Synthetic Biology, Shenzhen Institute of Advanced Technology, Chinese Academy of Sciences, Shenzhen 518055, People's Republic of China; and [h]National Laboratory of Biomacromolecules, Institute of Biophysics, Chinese Academy of Sciences, Beijing 100101, People's Republic of China

Edited by David Baker, Institute for Protein Design, University of Washington, Seattle, WA; received March 14, 2021; accepted November 18, 2021

Protein nanocages (PNCs) in cells and viruses have inspired the development of self-assembling protein nanomaterials for various purposes. Despite the successful creation of artificial PNCs, the de novo design of PNCs with defined permeability remains challenging. Here, we report a prototype oxygen-impermeable PNC (OIPNC) assembled from the vertex protein of the β-carboxysome shell, CcmL, with quantum dots as the template via interfacial engineering. The structure of the cage was solved at the atomic scale by combined solid-state NMR spectroscopy and cryoelectron microscopy, showing icosahedral assembly of CcmL pentamers with highly conserved interpentamer interfaces. Moreover, a gating mechanism was established by reversibly blocking the pores of the cage with molecular patches. Thus, the oxygen permeability, which was probed by an oxygen sensor inside the cage, can be completely controlled. The CcmL OIPNC represents a PNC platform for oxygen-sensitive or oxygen-responsive storage, catalysis, delivery, sensing, etc.

protein cages | quantum dots | oxygen permeability | templated assembly | solid-state NMR

Protein nanocages (PNCs), which are widely found in the biosphere, are well-organized structures formed through self-assembly. They provide compartments for enzyme-catalyzed reactions (1, 2), delivery (3), and storage (4) and have inspired the design of self-assembling protein nanomaterials. Considerable achievements in the design and assembly of PNCs with defined symmetry, size, and stability have been reported (5–7). However, little attention has been given to the creation of PNCs with controllable permeability. In fact, permeability is a key characteristic that can dictate or influence the functionality of PNCs (4, 8). Carboxysome, a representative PNC, is a protein-based organelle that is the site of carbon fixation in all cyanobacteria and some chemoautotrophic bacteria (2). It encapsulates the enzymes carbonic anhydrase and ribulose 1,5-bisphosphate carboxylase/oxygenase in a shell structure. This shell serves as a selective diffusion barrier that allows HCO_3^- to access the lumen while preventing escape of CO_2 (9) and possibly limiting entry of O_2, thereby considerably improving carbon sequestration efficiency (10). The carboxysome shell resembles an icosahedral viral capsid, with facets composed of hexameric and trimeric protein building blocks and vertices capped by pentameric proteins (2). The ordered assembly of these shell proteins is the structural basis of the selective permeability of these systems. The carboxysome inspires the construction of O_2-impermeable PNCs (OIPNCs) with self-assembling proteins, which introduces possibilities for the design and fabrication of novel materials and nanodevices and may help to clarify the working principles of natural protein organelles. For example, some O_2-sensitive bioprobes (11) and clinical drugs (12) are particularly effective but face severe stability problems or side effects due to reactions with O_2; some enzymes are extremely O_2-sensitive and can be irreversibly inactivated by O_2 (13, 14). OIPNCs can serve as a platform for solving such problems.

Taking carboxysomes as an example, one strategy is the reconstruction of carboxysomes via synthetic biology methods in different systems such as bacteria (15) and plants (16). Previous attempts have resulted in shell-like structures assembled from multiple or all recombinant carboxysome proteins (17–19). However, controlling the assembly and functionalization of carboxysome-derived cages is difficult due to their structural complexity. Probing the O_2 impermeability of these cages is equally challenging. Another strategy is the construction of simplified OIPNCs through the de novo assembly of a single kind of shell protein from carboxysomes. Working with a simplified OIPNC is expected to be more predictable and more convenient

Significance

Design of nanostructured protein materials is a big challenge due to structural complexity. Even more challenging is the design of protein nanomaterials endowed with specific properties and functions. Here, we report a prototype oxygen-impermeable protein nanocage assembled from the pentameric vertex protein of β-carboxysomes, CcmL, through nanoparticle templating. We solved the structure of the cage at the atomic scale by integrating solid-state NMR spectroscopy and cryoelectron microscopy and designed a molecular patch to the pores of the cage based on the structure, establishing a gating mechanism for reversible control of the oxygen permeability. The CcmL cage can serve as a protein nanoplatform for oxygen-sensitive or -responsive storage, catalysis, delivery, sensing, etc.

Author contributions: H.T., J.Y., X.-E.Z., and F.L. designed research; R.G., S.L., S.M., Y.T., and K.Z. performed research; Z.Z., Q.F., and F.L. contributed new reagents/analytic tools; R.G., H.T., S.L., S.M., Y.T., K.Z., Z.Z., Q.F., J.Y., X.-E.Z., and F.L. analyzed data; and R.G., H.T., S.L., J.Y., X.-E.Z., and F.L. wrote the paper.

The authors declare no competing interest.

This article is a PNAS Direct Submission.

[1]R.G., H.T., and S.L. contributed equally to this work.

[2]To whom correspondence may be addressed. Email: fli@wh.iov.cn, yangjun@wipm.ac.cn, or zhangxe@ibp.ac.cn.

This article contains supporting information online at http://www.pnas.org/lookup/suppl/doi:10.1073/pnas.2104964119/-/DCSupplemental.

Published January 25, 2022.

both for controlled assembly and for further engineering. A major challenge in this strategy is how to establish interfacial interactions between shell proteins to achieve uniform assembly and controllable permeability.

Here, we report a prototype OIPNC assembled through nanoparticle templating of the pentameric vertex protein of the β-carboxysome from *Thermosynechococcus elongatus* BP-1, CcmL. CcmL pentamers can assemble into uniform cage–like structures with quantum dots (QDs) as the template through protein–QD interfacial engineering. The ordered assembly of CcmL pentamers around QDs has been observed in detail by solid-state NMR (ssNMR) spectroscopy and cryoelectron microscopy (cryo-EM). Moreover, when probed by a QD O_2 sensor, the resultant cages show switchable permeability to O_2, which can be simply and reversibly controlled by molecular patches. This work represents a step toward the creation of artificial OIPNCs and lays the foundation for developing OIPNC-based nanodevices.

Results

QD-Templated Assembly of CcmL. In preliminary experiments, we found that recombinantly prepared CcmL can form non-uniform cage–like assemblies in vitro with low efficiency, suggesting that it has the potential to assemble into higher-order structures. The nanoparticle-templated assembly of proteins has been demonstrated to effectively guide or regulate the assembly of viral capsids (20), and nanoparticles can promote the assembly process by decreasing the kinetic barrier and shifting the minimum Gibbs free energy of the resultant protein cages (21). Therefore, we investigated whether the use of a nanoparticle template can guide the assembly of CcmL into uniform cage structures. We chose CdSe/ZnS core/shell QDs as the template for two reasons: the protein–QD interactions can be conveniently tuned by histidine–Zn coordination, and a fluorescent QD can function as an intrinsic O_2 sensor (22).

The structure of the CcmL pentamer resembles a truncated pentagonal pyramid (Fig. 1*A*) (24). When incubated with QDs at a pentamer/QD molar ratio of 10:1, CcmL bound to the QDs, as observed by transmission electron microscopy (TEM). After separation of these CcmL-QD complexes using sucrose density gradient centrifugation (SDGC), a band with the typical QD color (orange) appeared in fraction 6 (F6) in the SDGC tube (Fig. 1*B*), while free QDs in the control tube were bound to the wall and precipitated at the bottom of the SDGC tube due to aggregation (*SI Appendix*, Fig. S1). Analysis of the 10 fractions collected from the top to the bottom of the SDGC tube by sodium dodecyl sulfate–polyacrylamide gel electrophoresis (SDS-PAGE) showed that CcmL was present mainly in F1, F2, and F6 (Fig. 1*C*). The colocalization of CcmL and QDs and the stabilization of QDs supported the interactions between CcmL and QDs. However, TEM observations revealed that the purified CcmL-QD complex in F6 was more like products of nonspecific binding than protein cages (Fig. 1*D*).

To induce assembly of CcmL onto QDs with a controlled orientation, we genetically engineered CcmL by inserting a penta-histidine tag (Histag) between D33 and G34 in a loop localized in the concave region of the pentamer (Fig. 1*F* and *SI Appendix*, Fig. S2), taking advantage of the well-known metal–histidine coordination behavior (25). After incubation of the mutated CcmL (HCcmL) with QDs, the mixture was analyzed via a process similar to that used for CcmL-QD (Fig. 1 *G–I*). Although QDs also appeared in F6 (Fig. 1*G*), HCcmL was primarily distributed in F6 (Fig. 1*H*), which was different from the distribution of CcmL. According to the TEM observations, samples from F6 contained uniform protein particles with a QD core (QD@HCcmL), which showed a narrow size distribution and a mean diameter of 12.5 ± 1.2 nm (Fig. 1*I*). Dynamic light scattering (DLS) analysis also showed a narrow size distribution of QD@HCcmL, with the hydrodynamic diameter peaking at 14.9 nm (*SI Appendix*, Fig. S3). In addition, interaction analysis using biolayer interferometry (BLI) revealed a 10^2-fold higher affinity between HCcmL and QDs than between CcmL and QDs (Fig. 1 *E* and *J*). These data confirmed that uniform QD@HCcmL assemblies were formed, in which the inserted Histag played an important role in regulating the CcmL-QD interactions.

Structural Identification of the HCcmL Pentamer in QD@HCcmL by ssNMR Spectroscopy. To determine whether the templated assembly of HCcmL is ordered and explore the assembly mechanism, we first tried to solve the structure of the QD@HCcmL assembly by ssNMR spectroscopy. The two-dimensional (2D) ^{15}N-$^{13}C\alpha$ (NCA) correlation spectra of uniformly ^{13}C,^{15}N-labeled (U-^{13}C,^{15}N) QD@HCcmL and free HCcmL were collected first and showed good resolution (Fig. 2*A*), indicating that the conformations of HCcmL were highly homogeneous in both samples. Notably, the observation of only one set of resonances also suggests that all the HCcmL monomers in QD@HCcmL are symmetry equivalent, similar to the case of inflammasome assembly (26). The superposition of the NCA spectra of QD@HCcmL and free HCcmL showed similar chemical shift for most signals, suggesting that the structure of HCcmL did not significantly change after coassembly with QDs. To assign the resonances, we collected a set of three-dimensional (3D) CONCA, NCACX, and NCOCX (27) spectra of U-^{13}C,^{15}N–labeled HCcmL and QD@HCcmL (*SI Appendix*, Fig. S4). We assigned 72 resonances for both samples based on these dipolar coupling-based experiments, while the other 32 residues gave no signal, probably due to their high flexibility (Fig. 2*B* and *SI Appendix*, Table S1). All the assigned residues, except residues H70 and T75 in the two samples, have similar chemical shifts. R92 gave a signal in the spectrum of HCcmL but no signal in the spectrum of QD@HCcmL (*SI Appendix*, Table S2). Moreover, it is worth noting that Histags H34 through H38 exhibited five individual peaks in the NCA spectrum of QD@HCcmL but only one broad peak in the spectrum of free HCcmL (Fig. 2*A*). This difference is indicative of the interactions between the Histag and QDs and agrees well with the results of the BLI affinity measurements. The resonance assignments also allowed us to predict the secondary structure and torsion angles of QD@HCcmL by TALOS+ (28) (Fig. 2*C*).

To further elucidate the tertiary structure of HCcmL, ^{13}C-^{13}C distance constraints were obtained from a series of 2D ^{13}C-^{13}C proton-driven spin diffusion (PDSD) spectra of 2-^{13}C-glycerol–labeled HCcmL and QD@HCcmL with different PDSD mixing times (*SI Appendix*, Fig. S5). Before the analysis, we examined whether HCcmL maintained its pentameric conformation in the QD@HCcmL assembly. Size-exclusion chromatography confirmed that the HCcmL dissociated from the QD@HCcmL sample maintained a pentameric state similar to those of CcmL and HCcmL directly purified from *Escherichia coli* (*SI Appendix*, Fig. S6). Therefore, the signals in the PDSD spectra may correspond to intramonomer, intermonomer, and interpentamer contacts. Next, we used the following strategy to differentiate these constraints. First, most intramonomer and nonintramonomer restraints can be differentiated by a monomer structure model (*SI Appendix*, Fig. S7), which was predicted by CS-Rosetta (29) using chemical shift assignments, several unambiguous distance constraints, and homology modeling based on Kerfeld's high-resolution X-ray structure of CcmL (23). Second, interpentamer and noninterpentamer constraints can be differentiated by comparing the PDSD spectra of HCcmL and QD@HCcmL, since interpentamer contacts are expected to be present only in the spectra of QD@HCcmL (*SI Appendix*, Fig. S8). As a result, we obtained 317 intramonomer and 19 intermonomer distance constraints that were unambiguous

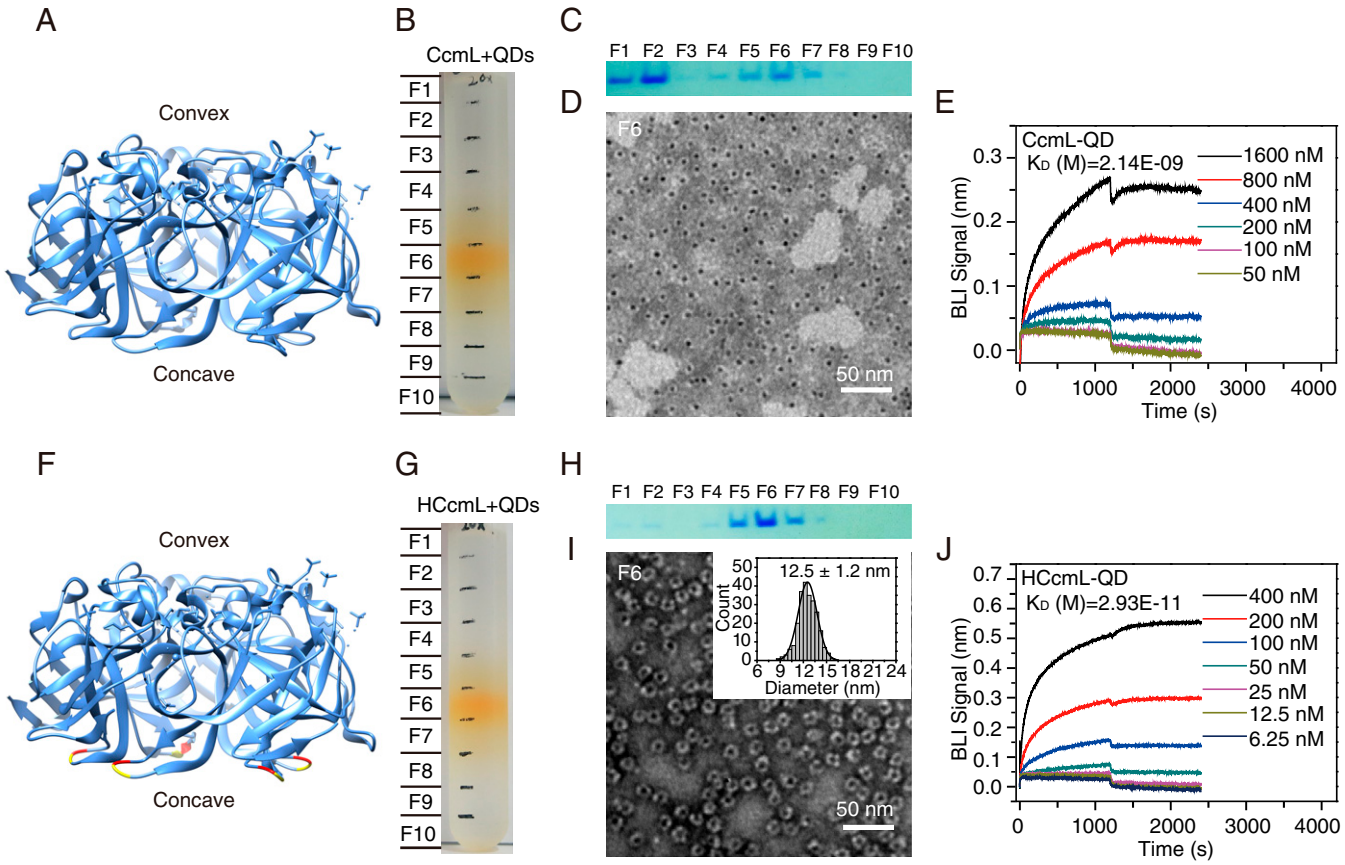

Fig. 1. Comparison of the assemblies between CcmL/HCcmL and QDs (CdSe/ZnS). (*A*) The 3D crystal structure of the CcmL pentamer [PDB: 4JVZ (23)], viewed from the side. (*B*) Image of an SDGC tube after separation of the CcmL-QD complex. The sample was separated into 10 fractions (F1 through F10) from the top to the bottom of the tube. (*C*) Distribution of CcmL in F1 through F10 as analyzed by SDS-PAGE and Coomassie blue staining. (*D*) TEM image of the CcmL-QD complex in F6. (*E*) Affinity measurement curves for the interactions between the CcmL pentamer and QD by BLI. (*F*) Model of HCcmL in which a Histag was inserted between D33 (red) and G34 (yellow) of every CcmL protomer. (*G*) Image of the tube of HCcmL-QD–coassembled products after separation by SDGC. (*H*) Distribution of HCcmL in F1 through F10 as analyzed by SDS-PAGE after SDGC. (*I*) TEM image of the QD@HCcmL harvested from F6. The inset in the upper right shows the diameter distribution based on TEM data (~240 particles). (*J*) Affinity measurement curves for the interactions between the HCcmL pentamer and QD by BLI.

(*SI Appendix*, Table S3). Interpentamer contacts were not observed by ssNMR spectroscopy, probably due to static structural disorder at the interpentamer interfaces, which can cause diminished resonance intensity (30).

Using intramonomer distance constraints (Fig. 3*A*) and torsion angle constraints (Fig. 2*C*), we calculated the HCcmL monomer structure in QD@HCcmL (Fig. 3 *B*, *Left*) by a standard calculation method, Xplor-NIH (31). As shown in Fig. 3*A*, interresidue antiparallel contacts between neighboring strands, such as W59-I87, V60-I86, and V84-S63, were used to refine the "basket" structure consisting of six β-sheets (enclosed by the dotted circle in Fig. 3 *B*, *Left*). Alignment of the calculated HCcmL monomer structure in QD@HCcmL with the crystal structure of the CcmL monomer showed similar folds (Fig. 3 *B*, *Right*), indicating that neither introduction of the Histag nor coassembly with QDs significantly changed the structure of CcmL. Moreover, unambiguously assigned intermonomer constraints (Fig. 3*C*) were used to identify the intermonomer interfaces (Fig. 3*D*). Using these intermonomer distance constraints and the monomer structure, we obtained highly convergent HCcmL pentamer structures with 0.5 Å rmsd in the backbone and 1.4 Å rmsd among all heavy atoms (Fig. 3 *E*, *Left* and *SI Appendix*, Fig. S9 and Table S3). In the structure determined by ssNMR spectroscopy, the artificially introduced Histags were at the bottom of the HCcmL pentamer, forming an open "claw" for grasping the QD core (Fig. 3 *E*, *Left*). Furthermore, the segments (marked with red in Fig. 3*B*) on both sides of H34 through H38 were likely relatively flexible, since their signals were not observed in dipolar coupling-based experiments. The flexibility of these segments made it easier for H34 through H38 to fit to the QD surface, facilitating the assembly of QD@HCcmL. Compared to the crystal structure (Protein Data Bank [PDB]: 4JVZ) of CcmL, the ssNMR structure of the HCcmL pentamer in the hybrid assembly appears looser, with more random loop regions (Fig. 3 *E*, *Right*). The differences between the ssNMR and X-ray structures should be attributed to the five introduced His residues and their interactions with QDs in QD@HCcmL.

Structural Model of QD-Templated HCcmL Nanocage Solved by Integrating ssNMR and Cryo-EM. To characterize the arrangement of HCcmL pentamers around the QDs, cryo-EM single-particle analysis was used to reconstruct the QD@HCcmL assemblies. Over 55,000 particles were selected for 3D refinement after several rounds of 2D classification (Fig. 4*A* and *SI Appendix*, Fig. S10). Because of the high density and nonspecific shape of the QDs, the overall reconstruction was not well resolved. By subtracting the signal of the QD density and focusing on the refinement of the outer cage (Fig. 4*B* and *SI Appendix*, Fig. S10), we were able to obtain a good 3D reconstruction. Even without applying symmetry operations during the reconstruction (Fig. 4 *C*, *Left*), the 3D map showed global icosahedral symmetry, which was consistent with the observation of

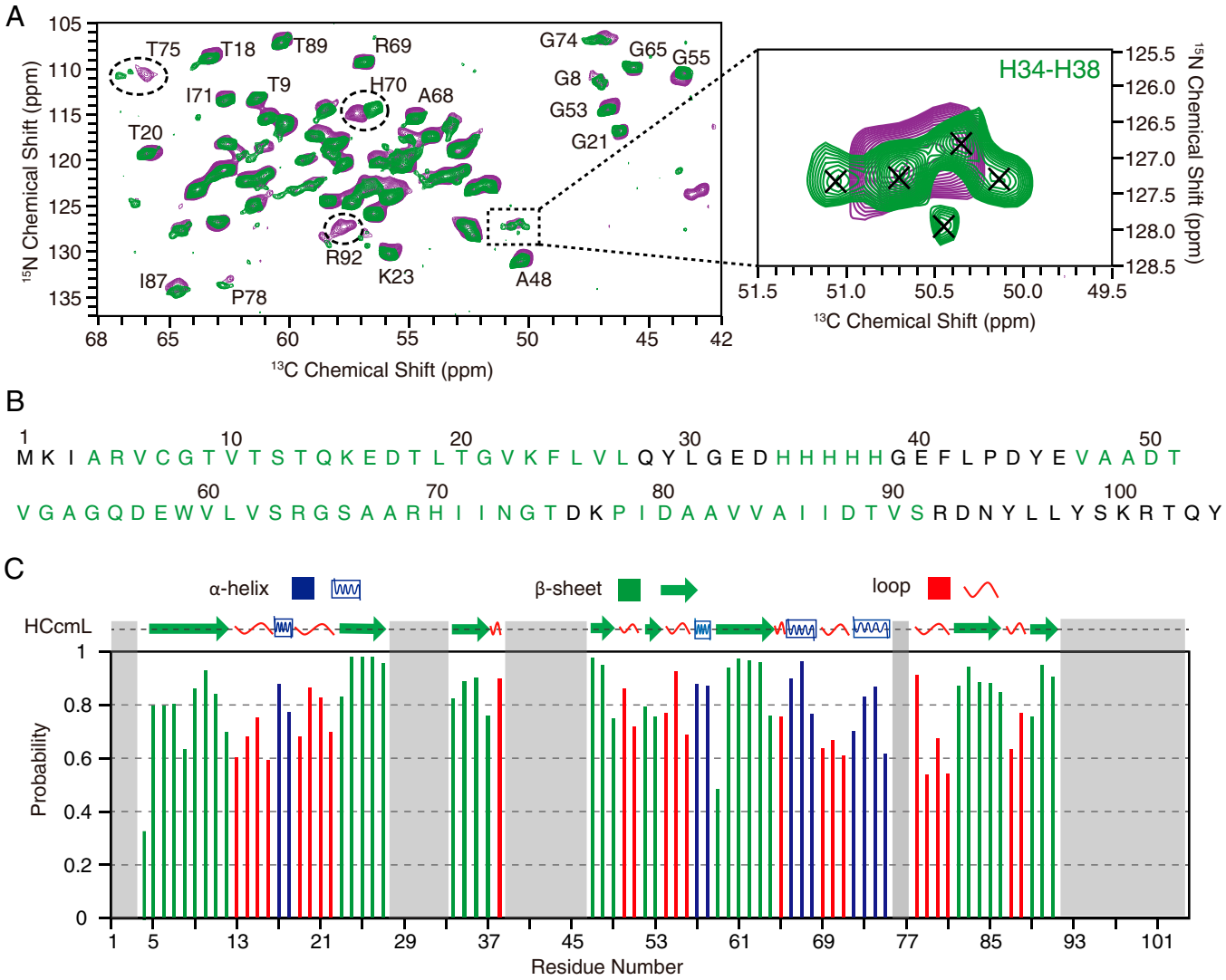

Fig. 2. Comparison of the ssNMR spectra of free and assembled HCcmL and the secondary structure of HCcmL in QD@HCcmL. (*A*) Superposition of the 2D NCA spectra of HCcmL (purple) and QD@HCcmL (green). The signals with substantially different chemical shifts or intensities are enclosed by dashed lines. (*B*) The amino acid sequence of HCcmL in QD@HCcmL, in which the residues assigned and unassigned by dipolar coupling-based experiments are shown in green and black, respectively. (*C*) The probability of secondary structure prediction calculated by TALOS+ based on the chemical shifts. The residues not detected by dipolar coupling-based experiments are shown in gray.

only one set of ssNMR resonances, as discussed above (Fig. 2). Further refinement with icosahedral symmetry achieved a 9.2-Å cryo-EM map (Fig. 4 *C*, *Right*, Fig. 4*D*, and *SI Appendix*, Fig. S10). The final maps with and without icosahedral symmetry applied were very similar, with a cross-correlation coefficient of 0.82 (*SI Appendix*, Figs. S11 and S12). The diameter of the cage from the cryo-EM map was ∼14.0 nm, consistent with the DLS results shown in *SI Appendix*, Fig. S3. The cryo-EM results further confirmed the formation and stability of the QD@HCcmL cage at the subnanometer scale.

Combining the structural information obtained from ssNMR spectroscopy and cryo-EM with all-atom molecular dynamics simulations has been proven to be a powerful strategy for solving the structures of biological or synthetic molecules (26, 32). Therefore, we fitted the cryo-EM map with the ssNMR pentamer structure using molecular dynamics flexible fitting (MDFF) (33) (Fig. 4*E*). The final model fit the experimental map remarkably well, with an overall cross-correlation coefficient of 0.93, which was quite similar to the simulation results (0.96) for the HIV-1 capsid (34). By using this model, we analyzed the residues involved in the interpentamer interfaces in QD@HCcmL. The assembly had well-conserved interpentamer interfaces that were mainly composed of residues T9, V10, D33 through H36, E40 through L42, W59, and D88 through R92 (Fig. 4*F*), of which T9, H34, H35, H36, F41, W59, T89, V90, S91, and R92 were highly conserved at all interpentamer interfaces (Fig. 4*G*), confirming the ordered organization of HCcmL around the QD template. We further statistically analyzed the types of interactions between these conserved residues and found that hydrogen bonds were the dominant type of interactions at the interfaces (*SI Appendix*, Fig. S13*A* and Table S4), which was similar to what was observed at the interfaces in HIV capsid protein hexamer arrays (35). In particular, 40% of the total hydrogen bonds were estimated to involve the artificially introduced Histag (H34, H35, and H36), and these His residues served as both proton donors and proton acceptors (*SI Appendix*, Fig. S13*B*). Therefore, the critical role of the Histag in the orderly assembly of HCcmL lies not only in its interactions with the QDs but also in its involvement in the hydrogen-bond network at the interpentamer interfaces. We

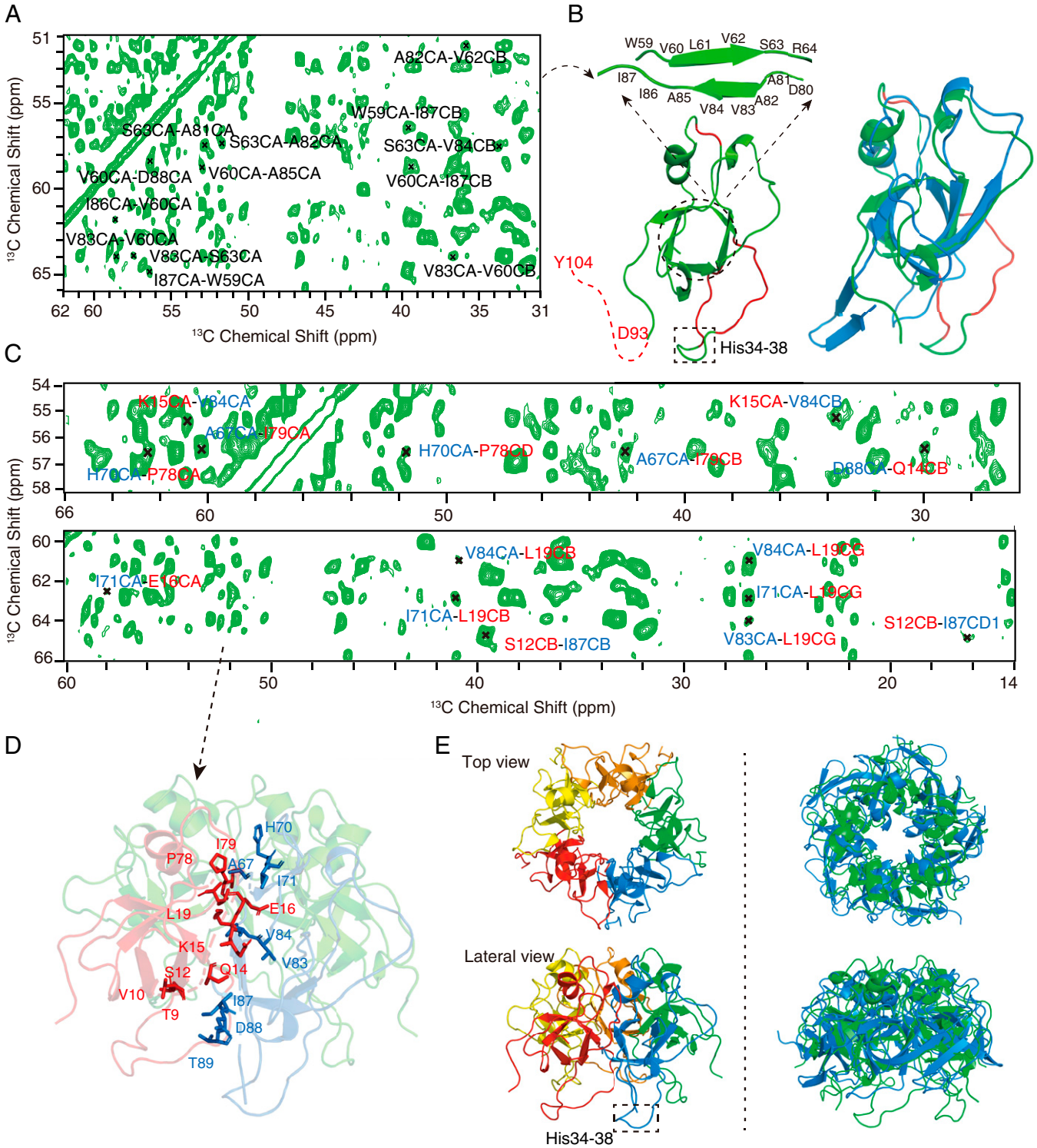

Fig. 3. ssNMR structural determination of the HCcmL pentamer in QD@HCcmL. (*A*) The 2D ^{13}C-^{13}C correlation spectrum with a PDSD mixing time of 500 ms for 2-^{13}C-glycerol–labeled QD@HCcmL. The signals corresponding to intramonomer distance restraints for refining the antiparallel arrangement of the neighboring strands, as shown in *B*, are marked. (*B*, *Left*) HCcmL monomer structure in QD@HCcmL determined by ssNMR spectroscopy. The fragments observed and not observed by dipolar coupling-based experiments are shown in green and red, respectively. (*Right*) Superposition of the HCcmL monomer (green) and CcmL monomer (blue, PDB: 4JVZ). (*C* and *D*) The 2D ^{13}C-^{13}C correlation spectrum with a PDSD mixing time of 500 ms for 2-^{13}C-glycerol–labeled QD@HCcmL (*C*), in which the signals corresponding to the intermonomer distance restraints for refining intermonomer interface (*D*) are marked. (*E*, *Left*) The structure of the HCcmL pentamer in QD@HCcmL calculated using ssNMR restraints. Each monomer is shown in a different color. (*Right*) Superposition of the HCcmL pentamer (green) and CcmL pentamer (blue, PDB: 4JVZ) shown in different orientations.

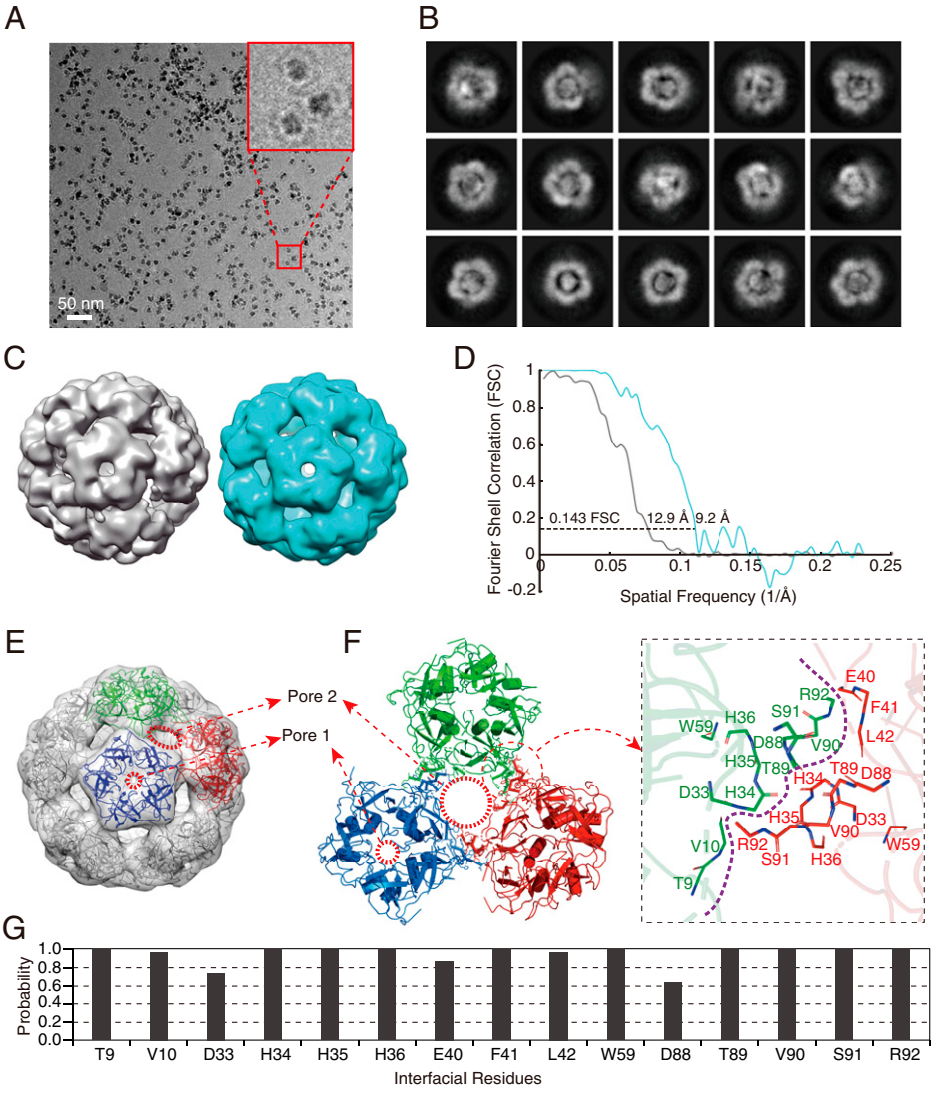

Fig. 4. Structural determination of QD@HCcmL by a hybrid method combining ssNMR spectroscopy and cryo-EM. (*A*) Representative motion-corrected cryo-EM micrograph of QD@HCcmL with a zoomed-in view of a few representative particles at top right corner (red box). (*B*) Reference-free 2D class averages after particle subtraction of QDs. (*C*) Final 3D reconstruction with (*Right*) and without (*Left*) refinement using icosahedral symmetry. (*D*) Gold-standard Fourier shell correlation plots for the final 3D reconstruction. (*E*) Fitting of the ssNMR pentamer structure into a cryo-EM map using molecular dynamics flexible fitting. The HCcmL pentamer central pores and pores surrounded by HCcmL pentamers were named pore 1 and pore 2, respectively. (*F*) Interpentamer interfaces in the HCcmL cage (*E*), mainly containing amino acids T9, V10, D33 through H36, E40 through L42, W59, and D88 through R92. (*G*) The probability of amino acid residues appearing at each interpentamer interface of the QD@HCcmL assembly.

speculate that H37 and H38 mainly interact with the QDs, while H34, H35, and H36 mediate the ordered arrangement of the interpentamer interfaces.

The structural model of the nanocage demonstrates that the convex region of the HCcmL pentamer faces outward. Such an orientation is opposite to what is observed in carboxysomes (36). Actually, this orientation was expected at the beginning of this study. In a preliminary experiment, we found that the coassembly efficiency of CcmL and QDs was lower when the Histag was inserted into the convex region of the CcmL pentamer than when it was inserted into the concave region. Therefore, we chose the mutant with the Histag inserted into the concave region (Fig. 1*F*).

Control of the O_2 Permeability of the QD-Templated HCcmL Cage. To explore whether the QD-templated HCcmL cage is O_2 impermeable, we first analyzed its structure. Two types of pores were observed in the shell of the cage. Type-1 pores were present at the fivefold axis of symmetry in the HCcmL pentamers (pore 1, Fig. 4*E*), and type-2 pores were observed at the threefold axis of symmetry in the cage (pore 2, Fig. 4*E*). According to measurements using Hole software (37), both types of pores have size distributions (*SI Appendix*, Fig. S14) with average diameters of ~4.0 Å for pore 1 and ~14.0 Å for pore 2. Although the size of pore 1 is a bit larger than that of O_2 [3.46 Å (38)], it is positively charged (*SI Appendix*, Fig. S15) and thus does not attract nonpolar molecules such as O_2 (39). Moreover, hydration of pore 1 causes steric hindrance to the transit of O_2 molecules. Therefore, pore 1 is thought to be O_2 impermeable (see detailed description in *Discussion*). The average size of pore 2 is much larger than that of O_2, suggesting that type-2 pores could physically allow O_2 to enter the cage. However, type-2 pores could potentially be used as gates to regulate the O_2 permeability of the HCcmL cage with molecular patches.

To experimentally test this hypothesis, we next measured the O_2 permeability of the HCcmL cage with O_2-sensitive CdS/ZnS core/shell QDs as the probe. The responses of the QDs to

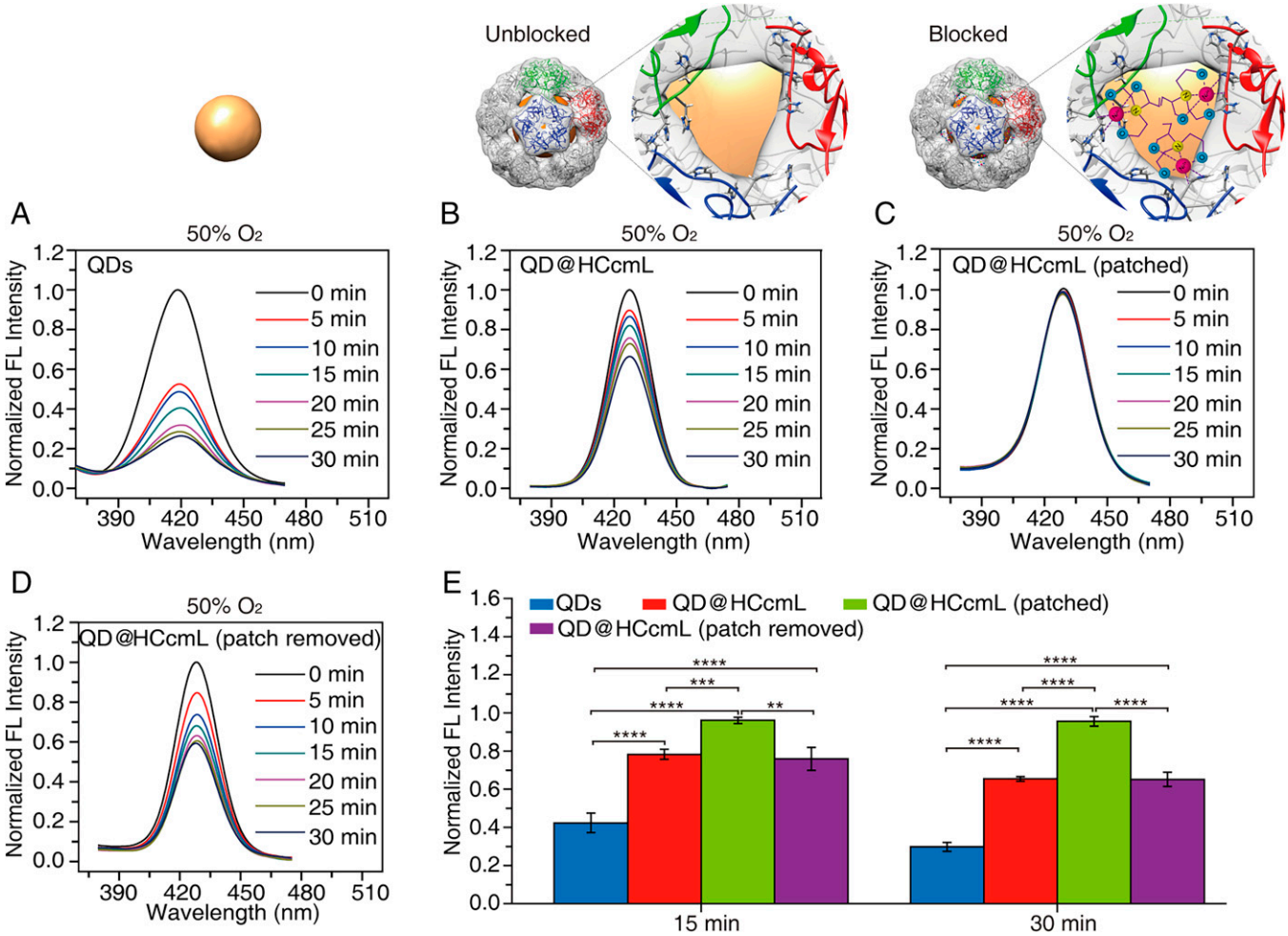

Fig. 5. Responses of the O_2-sensitive QDs (CdS/ZnS), QD@HCcmL, QD@HCcmL (patched), and QD@HCcmL (patch removed) to O_2 treatment. (*A–D*) Fluorescence (FL) spectra of QDs (*A*), QD@HCcmL with unblocked type-2 pores (*B*), QD@HCcmL (patched) (*C*), and QD@HCcmL (patch removed) (*D*) upon treatment with 50% O_2 for 30 min. (*E*) Histogram of the fluorescence intensities of QDs, QD@HCcmL, QD@HCcmL (patched), and QD@HCcmL (patch removed) after 15 or 30 min of treatment with 50% O_2. Data were normalized to the fluorescence values of the corresponding samples at 0 min and represent means ± SDs from three independent replicates. $^{**}P < 0.01$; $^{***}P < 0.001$; and $^{****}P < 0.0001$. Statistical significance was assessed by one-way ANOVA followed by Fisher's least significant difference (LSD) test.

O_2 were examined by fluorescence measurements with different parameters, and the results showed both exposure time–dependent and O_2 level–dependent fluorescence decrease (Fig. 5*A* and *SI Appendix*, Figs. S16*A* and S17). These results confirmed the feasibility of using QDs as an O_2 probe. After formation of the QD@HCcmL complexes (*SI Appendix*, Fig. S18), the fluorescence of the QDs became less sensitive to O_2 exposure. Specifically, after treatment of the samples with 50% O_2 for 30 min, the fluorescence of the QDs in the HCcmL cages was quenched to 65.4% of its initial value (at 0 min) (Fig. 5 *B* and *E* and *SI Appendix*, Fig. S16*B*), while that of free QDs decreased to 29.7% at equivalent QD concentrations (Fig. 5 *A* and *E* and *SI Appendix*, Fig. S19). Due to the presence of type-2 pores, the cages were not predicted to be impermeable; however, the results suggest that the HCcmL cages could partially protect the QDs from O_2 even if they have pores larger than O_2. This partial protection can be attributed to the close interaction between HCcmL pentamers and the QD surface revealed by the high-resolution structural analysis above (Figs. 3 and 4). The close protein–QD interaction prevented O_2 from freely diffusing within the cage, which is supported by O_2-sensing experiments with a small-molecule probe sandwiched between HCcmL pentamers and QDs (*SI Appendix*, *Supplementary Text* and Figs. S20–S29). A calculation of the quenching rate (QR) under conditions of enough O_2 gassing and the available surface area (SA) of QDs exposed by type-2 pores indicates that there is a good correlation between QR (35%) and SA (39%) (*SI Appendix*, *Supplementary Text* and Fig. S30), in agreement with the partial protection theory. In addition, two experiments with other proteins demonstrated that strongly adsorbed proteins on QDs can indeed protect QD fluorescence from O_2 quenching (*SI Appendix*, *Supplementary Text* and Fig. S31).

After determining that the HCcmL cage is O_2 permeable, probably due to the presence of type-2 pores, we then explored the possibility of tuning the cage to make it a true OIPNC by blocking the pores. Analysis of the residues surrounding pore 2 revealed an abundance of histidine residues. Therefore, we, on the basis of coordination chemistry, hypothesized that the pores could be blocked with Ni^{2+}-nitrilotriacetic acid (Ni-NTA). TEM observations showed no detectable changes in the morphology of QD@HCcmL after incubation with Ni-NTA (denoted as QD@HCcmL [patched]) (*SI Appendix*, Fig. S32). ssNMR analysis supports the proposed patching model. By comparing the 2D ^{13}C-^{13}C correlation spectra before and after Ni-NTA treatment (*SI Appendix*, Fig. S33*A*), we found that the paramagnetic relaxation enhancement (PRE) (40, 41) effect of Ni^{2+} resulted in the

disappearance of ssNMR signals of some residues (V6, C7, G21, V22, K23, V47, A48, G53, A54, A82, V83, V84, and A85) around the type-2 pore after Ni-NTA treatment (*SI Appendix*, Fig. S33*B*). The disappearance of these signals indicates the binding of Ni-NTA to the histidine residues around the type-2 pore. When these samples were challenged with 50% O_2, the fluorescence of QD@HCcmL (patched) showed almost no decrease (Fig. 5 *C* and *E* and *SI Appendix*, Fig. S16*C*), suggesting that the pores had been successfully blocked, forming an OIPNC. To test whether the blocking is reversible, we washed the QD@HCcmL (patched) particles with excess imidazole to remove the Ni-NTA patches and then remeasured the O_2 permeability. TEM characterization revealed that the morphology of QD@HCcmL after washing off the Ni-NTA (denoted as QD@HCcmL [patch removed]) remained intact (*SI Appendix*, Fig. S34). After treatment with 50% O_2 for 30 min, the fluorescence of QD@HCcmL (patch removed) decreased to 65.0% of the initial value (at 0 min) (Fig. 5 *D* and *E* and *SI Appendix*, Fig. S16*D*), which is similar to the case of QD@HCcmL before patching under the same O_2 treatment conditions. These results demonstrate that the HCcmL cage can serve as a nanocontainer whose O_2 permeability can be controlled by a gating mechanism.

Discussion

Permeability is an essential property of PNCs. Controlled permeability of PNCs is frequently observed in natural systems. In addition to carboxysomes, ferritins use pores to control iron flow (4), and tailed bacteriophage capsids utilize pore-based packaging machines for genome encapsidation and release (8, 42). In this study, we designed and fabricated a prototype OIPNC minimized from the multicomponent shell of β-carboxysome. The OIPNC is composed of only one kind of building block, the vertex protein of β-carboxysome (CcmL). To this end, we utilized QDs as templates for the assembly of CcmL pentamers, in which protein–QD interfacial interactions were engineered by inserting Histags into the concave region of the CcmL pentamer to achieve ordered assembly. Although a proportion of cages were somewhat distorted due to the nonspecific shape of the QD templates, the O_2-sensing experiment with pores blocked supports the idea that a HCcmL cage did form and covered the QD core, owing to the flexibility in interfacial interactions between HCcmL pentamers. Moreover, in the minimized OIPNC, a gating mechanism was established to easily control the O_2 permeability with a molecular patch such as Ni-NTA. This study represents an attempt to design PNCs with controllable molecular permeability.

Integration of inorganic nanomaterials and proteins is a common and important way to fabricate functional nanostructures through different techniques such as self-assembly (43), bioconjugation (44), and biomineralization (45). Although numerous kinds of such hybrid structures have been developed, solving the structure of proteins therein with atomic resolution remains a major challenge but is essential for understanding the inorganic-protein interfaces and structure–function relationships and guiding the design of hybrid structures. For instance, the resolution of protein structures solved by cryo-EM in hybrid assemblies of virus-like particles with inorganic nanoparticle cores was only ∼3 nm (20, 46). One reason for the difficulty is that X-ray crystallography is not possible for protein–inorganic hybrid complexes in most cases due to difficulties in crystallization. Another reason is that the strong electron density or nonspecific shape of the nanoparticle makes it difficult to obtain high-resolution electron density maps by cryo-EM. Fortunately, the integration of ssNMR spectroscopy and cryo-EM data allowed us to obtain an atomic-resolution structure of the HCcmL cage. Neither ssNMR spectroscopy nor cryo-EM require crystalline samples. Symmetry in the assembly usually results in uniform conformations of the local units, which allows characterization by ssNMR spectroscopy. ssNMR spectroscopy always provides atomic-level information regarding amino acids within a protein molecule, while a cryo-EM map allows us to determine the overall envelope of the assembly. The combination of these two techniques is an emerging method for solving protein structures with atomic resolution. In recent years, this combined method has been successfully applied to determine the structures of a few systems [e.g., the type-III secretion system needle (47), cyclophilin A (CypA) in complex with the HIV-1 capsid (48), and aminopeptidase TET2 (32)]. In contrast to these previous structures, which are composed of only organic biomolecules, HCcmL is coassembled with a 5-nm inorganic nanoparticle. Herein, we present an atomic-resolution structure of a protein assembly in inorganic nanoparticle-protein complexes, opening application possibilities of the combination of ssNMR spectroscopy and cryo-EM and highlighting the power of this emerging method.

On the basis of the structure of the HCcmL cage, two types of pores should be considered when investigating its permeability. In principle, the cage may be permeable to any molecule small enough to fit through the pores. However, we concentrate on the permeability to O_2 in this study. Although there is no direct experimental evidence in the literature that O_2 cannot pass through the central pore of the CcmL pentamer (corresponding to the type-1 pore in the HCcmL cage), there are findings that provide indirect information about this topic (49). Recent molecular dynamics simulation studies of the carboxysome shell hexamer proteins CsoS1A, CcmK4 (50), and CcmK2 (51) showed that the positive potential inside the pores facilitates passage of anions through the pores. However, although the pore sizes (4.0 Å or even larger in diameter) can accommodate a free small molecule such as O_2, it is difficult for such nonpolar molecules to pass through, as determined by the calculation of free energy (50, 51). The central pore of the CcmL pentamer is similar to those of the hexamer shell proteins (i.e., CsoS1A, CcmK4, and CcmK2) in terms of narrow size and positive potential (39). Therefore, the type-1 pore (4.0 Å in diameter) is probably O_2 impermeable. Our O_2-sensing experiment showed that the HCcmL protein cage is completely O_2 impermeable after blocking the type-2 pores with Ni-NTA. This supports the O_2 impermeability of the type-1 pore; otherwise, it might be also blocked by Ni-NTA. Dynamics of pores, as well as overall structures, has been described in many protein assembly systems and is crucial to their functions (52–55). According to the analysis of other carboxysome shell proteins (51), dynamic changes of the type-1 pore are possible upon binding of anions such as HCO_3^-, but the presence of O_2 is unlikely to trigger significant conformational changes in this region. The type-2 pores are much larger than O_2 molecules (14 Å versus 3.46 Å in size). Analysis of the residues surrounding these pores indicated that the pores could be blocked with molecular patches that have a high affinity for the abundant histidine residues, which led to a gating mechanism for reversibly controlling O_2 permeability. The success in establishing a gating mechanism for the artificial HCcmL nanocage, which is attributed to the understanding of its detailed structural features, will enhance the controllability of the protein nanotechnology platform.

In conclusion, a prototype OIPNC was constructed using the vertex protein of β-carboxysome as a building block and QDs as a template. The high-resolution structure obtained by a combination of ssNMR spectroscopy and cryo-EM confirmed the highly ordered assembly of the cage and enabled the design of a gating mechanism to control O_2 permeability, as demonstrated with a QD-based O_2 sensor. The nanoparticle templating strategy can be extended to other protein building blocks for de novo assembly of nanostructures, helping to establish interfacial interactions between proteins, like the way in which molecular chaperones work. This study also offers a paradigm

for solving the structures of proteins complexed with inorganic nanoparticles at atomic resolution, which will improve our understanding of protein–nanoparticle interactions and organization at an unprecedented depth. The O_2-probing strategies developed here may be useful for experimental studies of the O_2 permeability of bacterial microcompartments (BMCs), BMC-derived shells (56, 57), and other natural or artificial nanocontainers. The HCcmL cage here can only be called a prototype OIPNC, for it is not empty but contains a QD. Interpentamer interfacial interactions can be strengthened through genetic engineering to achieve efficient self-assembly of cages from CcmL. Also, understanding the structural dynamics of the cages and the ability to manipulate it deserve further endeavors. OIPNCs hold great potential in developing O_2-sensitive or O_2-responsive nanocontainers, nanoreactors, sensors, and carriers as well as nanocompartments in artificial cells (58).

Methods

Detailed methods are provided in *SI Appendix, SI Methods*. This includes detailed information about preparation and labeling of proteins, water solubilization of QDs, assembly of proteins and QDs, TEM, optical property measurements, measurement of affinity between proteins and QDs, DLS, ssNMR spectroscopy and data processing, structure calculations of HCcmL monomer and pentamer, cryo-EM, single-particle image processing and 3D reconstruction, MDFF, analysis of the HCcmL pentamer interfaces in QD@HCcmL cages, patching and patch removal of HCcmL cages, and O_2 sensing with QDs and Ir complex.

Data Availability. The cryo-EM structure of QD@HCcmL complex has been deposited to the Electron Microscopy Data Bank under accession code EMD-32549 (https://www.ebi.ac.uk/emdb/EMD-32549). The ssNMR structure of HCcmL pentamer has been deposited to the Biological Magnetic Resonance Bank and the Protein Data Bank under accession codes 36468 (https://bmrb.io/data_library/summary/index.php?bmrbId=36468) and 7WKC (https://www.rcsb.org/structure/7WKC). All study data are included in the article and/or *SI Appendix*.

ACKNOWLEDGMENTS. We are grateful for the financial support from the National Natural Science Foundation of China (Grant Nos. 31771103, 91527302, and 21425523), the Chinese Academy of Sciences (CAS) Emergency Project of African Swine Fever (ASF) Research (No. KJZD-SW-L06), the Strategic Priority Research Program of the CAS (No. XDB29050100), and the National Key Research and Development Program of China (Nos. 2017YFA0205500, 2016YFA0501200, and 2017YFA0505400). We thank Wenjing Zhang and Ming Li for providing the HisVP1 protein and Mengsi Yang for providing the His-Cas9 protein. We also thank Dr. Ding Gao and Pei Zhang at the Core Facility and Technical Support of the Wuhan Institute of Virology for assistance in TEM.

1. M. Comellas-Aragonès *et al.*, A virus-based single-enzyme nanoreactor. *Nat. Nanotechnol.* **2**, 635–639 (2007).
2. C. A. Kerfeld, C. Aussignargues, J. Zarzycki, F. Cai, M. Sutter, Bacterial microcompartments. *Nat. Rev. Microbiol.* **16**, 277–290 (2018).
3. A. M. Wen, N. F. Steinmetz, Design of virus-based nanomaterials for medicine, biotechnology, and energy. *Chem. Soc. Rev.* **45**, 4074–4126 (2016).
4. X. Liu, E. C. Theil, Ferritins: Dynamic management of biological iron and oxygen chemistry. *Acc. Chem. Res.* **38**, 167–175 (2005).
5. J. B. Bale *et al.*, Accurate design of megadalton-scale two-component icosahedral protein complexes. *Science* **353**, 389–394 (2016).
6. A. D. Malay *et al.*, An ultra-stable gold-coordinated protein cage displaying reversible assembly. *Nature* **569**, 438–442 (2019).
7. N. P. King *et al.*, Accurate design of co-assembling multi-component protein nanomaterials. *Nature* **510**, 103–108 (2014).
8. P. Tavares, S. Zinn-Justin, E. V. Orlova, "Genome Gating in tailed bacteriophage capsids" in *Viral Molecular Machines*, M. G. Rossmann, V. B. Rao, Eds. (Springer US, Boston, MA, 2012), pp. 585–600.
9. Z. Dou *et al.*, CO_2 fixation kinetics of *Halothiobacillus neapolitanus* mutant carboxysomes lacking carbonic anhydrase suggest the shell acts as a diffusional barrier for CO_2. *J. Biol. Chem.* **283**, 10377–10384 (2008).
10. C. A. Kerfeld, M. R. Melnicki, Assembly, function and evolution of cyanobacterial carboxysomes. *Curr. Opin. Plant Biol.* **31**, 66–75 (2016).
11. S. H. C. Askes, S. Bonnet, Solving the oxygen sensitivity of sensitized photon upconversion in life science applications. *Nat. Rev. Chem.* **2**, 437–452 (2018).
12. J. Chen, J. Stubbe, Bleomycins: Towards better therapeutics. *Nat. Rev. Cancer* **5**, 102–112 (2005).
13. J. Esselborn, L. Kertess, U. P. Apfel, E. Hofmann, T. Happe, Loss of specific active-site iron atoms in oxygen-exposed [FeFe]-hydrogenase determined by detailed X-ray structure analyses. *J. Am. Chem. Soc.* **141**, 17721–17728 (2019).
14. K. D. Swanson *et al.*, [FeFe]-hydrogenase oxygen inactivation is initiated at the H cluster 2Fe subcluster. *J. Am. Chem. Soc.* **137**, 1809–1816 (2015).
15. F. Cai, S. L. Bernstein, S. C. Wilson, C. A. Kerfeld, Production and characterization of synthetic carboxysome shells with incorporated luminal proteins. *Plant Physiol.* **170**, 1868–1877 (2016).
16. B. M. Long *et al.*, Carboxysome encapsulation of the CO_2-fixing enzyme Rubisco in tobacco chloroplasts. *Nat. Commun.* **9**, 3570 (2018).
17. M. T. Lin *et al.*, β-Carboxysomal proteins assemble into highly organized structures in Nicotiana chloroplasts. *Plant J.* **79**, 1–12 (2014).
18. Y. Fang *et al.*, Engineering and modulating functional cyanobacterial CO_2-fixing organelles. *Front. Plant Sci.* **9**, 739 (2018).
19. T. Li *et al.*, Reprogramming bacterial protein organelles as a nanoreactor for hydrogen production. *Nat. Commun.* **11**, 5448 (2020).
20. J. Sun *et al.*, Core-controlled polymorphism in virus-like particles. *Proc. Natl. Acad. Sci. U.S.A.* **104**, 1354–1359 (2007).
21. L. He, Z. Porterfield, P. van der Schoot, A. Zlotnick, B. Dragnea, Hepatitis virus capsid polymorph stability depends on encapsulated cargo size. *ACS Nano* **7**, 8447–8454 (2013).
22. W. Wang, L. Bao, J. Lei, W. Tu, H. Ju, Visible light induced photoelectrochemical biosensing based on oxygen-sensitive quantum dots. *Anal. Chim. Acta* **744**, 33–38 (2012).
23. M. Sutter, S. C. Wilson, S. Deutsch, C. A. Kerfeld, Two new high-resolution crystal structures of carboxysome pentamer proteins reveal high structural conservation of CcmL orthologs among distantly related cyanobacterial species. *Photosynth. Res.* **118**, 9–16 (2013).
24. T. O. Yeates, C. A. Kerfeld, S. Heinhorst, G. C. Cannon, J. M. Shively, Protein-based organelles in bacteria: Carboxysomes and related microcompartments. *Nat. Rev. Microbiol.* **6**, 681–691 (2008).
25. K. E. Sapsford *et al.*, Kinetics of metal-affinity driven self-assembly between proteins or peptides and CdSe–ZnS quantum dots. *J. Phys. Chem. C* **111**, 11528–11538 (2007).
26. L. Sborgi *et al.*, Structure and assembly of the mouse ASC inflammasome by combined NMR spectroscopy and cryo-electron microscopy. *Proc. Natl. Acad. Sci. U.S.A.* **112**, 13237–13242 (2015).
27. L. Shi *et al.*, Three-dimensional solid-state NMR study of a seven-helical integral membrane proton pump–structural insights. *J. Mol. Biol.* **386**, 1078–1093 (2009).
28. Y. Shen, F. Delaglio, G. Cornilescu, A. Bax, TALOS+: A hybrid method for predicting protein backbone torsion angles from NMR chemical shifts. *J. Biomol. NMR* **44**, 213–223 (2009).
29. Y. Shen *et al.*, Consistent blind protein structure generation from NMR chemical shift data. *Proc. Natl. Acad. Sci. U.S.A.* **105**, 4685–4690 (2008).
30. I.-J. L. Byeon *et al.*, Structural convergence between Cryo-EM and NMR reveals intersubunit interactions critical for HIV-1 capsid function. *Cell* **139**, 780–790 (2009).
31. C. D. Schwieters, J. J. Kuszewski, N. Tjandra, G. M. Clore, The Xplor-NIH NMR molecular structure determination package. *J. Magn. Reson.* **160**, 65–73 (2003).
32. D. F. Gauto *et al.*, Integrated NMR and cryo-EM atomic-resolution structure determination of a half-megadalton enzyme complex. *Nat. Commun.* **10**, 2697 (2019).
33. L. G. Trabuco, E. Villa, E. Schreiner, C. B. Harrison, K. Schulten, Molecular dynamics flexible fitting: A practical guide to combine cryo-electron microscopy and X-ray crystallography. *Methods* **49**, 174–180 (2009).
34. G. Zhao *et al.*, Mature HIV-1 capsid structure by cryo-electron microscopy and all-atom molecular dynamics. *Nature* **497**, 643–646 (2013).
35. A. T. Gres *et al.*, STRUCTURAL VIROLOGY. X-ray crystal structures of native HIV-1 capsid protein reveal conformational variability. *Science* **349**, 99–103 (2015).
36. M. Sutter *et al.*, Structure of a synthetic beta-carboxysome shell. *Plant Physiol.* **181**, 1050–1058 (2019).
37. O. S. Smart, J. G. Neduvelil, X. Wang, B. A. Wallace, M. S. Sansom, HOLE: A program for the analysis of the pore dimensions of ion channel structural models. *J. Mol. Graph.* **14**, 354–360, 376 (1996).
38. S. E. Kentish, C. A. Scholes, G. W. Stevens, Carbon dioxide separation through polymeric membrane systems for flue gas applications. *Recent Pat. Chem. Eng.* **1**, 52–66 (2008).
39. J. N. Kinney, S. D. Axen, C. A. Kerfeld, Comparative analysis of carboxysome shell proteins. *Photosynth. Res.* **109**, 21–32 (2011).
40. K. Aman, P. O. Westlund, The electron spin relaxation and paramagnetic relaxation enhancement: An application of the stochastic Liouville equation in the Langevin form. *Mol. Phys.* **102**, 1085–1093 (2004).
41. B. Liang, J. H. Bushweller, L. K. Tamm, Site-directed parallel spin-labeling and paramagnetic relaxation enhancement in structure determination of membrane proteins by solution NMR spectroscopy. *J. Am. Chem. Soc.* **128**, 4389–4397 (2006).
42. P. Jing, F. Haque, D. Shu, C. Montemagno, P. Guo, One-way traffic of a viral motor channel for double-stranded DNA translocation. *Nano Lett.* **10**, 3620–3627 (2010).
43. W. M. Aumiller, M. Uchida, T. Douglas, Protein cage assembly across multiple length scales. *Chem. Soc. Rev.* **47**, 3433–3469 (2018).

44. J. Zhou, Y. Yang, C. Y. Zhang, Toward biocompatible semiconductor quantum dots: From biosynthesis and bioconjugation to biomedical application. *Chem. Rev.* **115**, 11669–11717 (2015).
45. C.-Y. Wang *et al.*, Biological and synthetic template-directed syntheses of mineralized hybrid and inorganic materials. *Prog. Mater. Sci.* **116**, 100712 (2020).
46. F. Li *et al.*, Tunable, discrete, three-dimensional hybrid nanoarchitectures. *Angew. Chem. Int. Ed. Engl.* **50**, 4202–4205 (2011).
47. J. P. Demers *et al.*, High-resolution structure of the Shigella type-III secretion needle by solid-state NMR and cryo-electron microscopy. *Nat. Commun.* **5**, 4976 (2014).
48. C. Liu *et al.*, Cyclophilin A stabilizes the HIV-1 capsid through a novel non-canonical binding site. *Nat. Commun.* **7**, 10714 (2016).
49. Y. Marcus, J. A. Berry, J. Pierce, Photosynthesis and photorespiration in a mutant of the cyanobacterium Synechocystis PCC 6803 lacking carboxysomes. *Planta* **187**, 511–516 (1992).
50. P. Mahinthichaichan, D. M. Morris, Y. Wang, G. J. Jensen, E. Tajkhorshid, Selective permeability of carboxysome shell pores to anionic molecules. *J. Phys. Chem. B* **122**, 9110–9118 (2018).
51. M. Faulkner *et al.*, Molecular simulations unravel the molecular principles that mediate selective permeability of carboxysome shell protein. *Sci. Rep.* **10**, 17501 (2020).
52. L. Zubcevic *et al.*, Cryo-electron microscopy structure of the TRPV2 ion channel. *Nat. Struct. Mol. Biol.* **23**, 180–186 (2016).
53. J. Yoo *et al.*, Cryo-EM structure of a mitochondrial calcium uniporter. *Science* **361**, 506–511 (2018).
54. F. Tama, C. L. Brooks, 3rd, Diversity and identity of mechanical properties of icosahedral viral capsids studied with elastic network normal mode analysis. *J. Mol. Biol.* **345**, 299–314 (2005).
55. M. Karplus, J. A. McCammon, Dynamics of proteins: Elements and function. *Annu. Rev. Biochem.* **52**, 263–300 (1983).
56. F. Cai, M. Sutter, S. L. Bernstein, J. N. Kinney, C. A. Kerfeld, Engineering bacterial microcompartment shells: Chimeric shell proteins and chimeric carboxysome shells. *ACS Synth. Biol.* **4**, 444–453 (2015).
57. A. R. Hagen *et al.*, In vitro assembly of diverse bacterial microcompartment shell architectures. *Nano Lett.* **18**, 7030–7037 (2018).
58. B. Wörsdörfer, K. J. Woycechowsky, D. Hilvert, Directed evolution of a protein container. *Science* **331**, 589–592 (2011).